medRxiv preprint doi: https://doi.org/10.64898/2026.06.21.26356164; this version posted June 23, 2026. The copyright holder for this preprint (which was not certified by peer review) is the author/funder, who has granted medRxiv a license to display the preprint in perpetuity.
It is made available under a CC-BY-NC 4.0 International license .

Post Hoc Localization of Beam F3 Stimulation Targets: An MRI-Derived Geodesic Approach for Refined TMS E-Field Simulations

Severin Schramm[1,2,3]; Julia Ten Pas[1]; Daniele Calabrò[1]; Julia Jakubetz[1]; Malte Szillat[1]; Joan Koti[4]; Minyan Huang[5]; Su Hwan Kim[1]; Michael Woletz[5]; Jan Kirschke[1]; Dennis M. Hedderich[1]; Nico Sollmann[1,6,7,8]; Martin Tik[5] & Ulrike Vogelmann[2,4]

[1] Institute for Diagnostic and Interventional Neuroradiology, School of Medicine and Health, TUM Klinikum rechts der Isar, Technical University of Munich, Munich, Germany;

[2] German Center for Mental Health (DZPG), partner site München-Augsburg, Germany;

[3] Institute for Cardiovascular Radiology and Nuclear Medicine, German Heart Center Munich, School of Medicine and Health, Technical University of Munich, Munich, Germany;

[4] Clinic and Policlinic for Psychiatry and Psychotherapy, School of Medicine and Health, TUM Klinikum rechts der Isar, Technical University of Munich, Munich, Germany;

NOTE: This preprint reports new research that has not been certified by peer review and should not be used to guide clinical practice.

medRxiv preprint doi: https://doi.org/10.64898/2026.06.21.26356164; this version posted June 23, 2026. The copyright holder for this preprint (which was not certified by peer review) is the author/funder, who has granted medRxiv a license to display the preprint in perpetuity.
It is made available under a CC-BY-NC 4.0 International license .

[5] MR Center of Excellence, Center for Medical Physics and Biomedical Engineering, Medical University of Vienna, Vienna, Austria;

[6] TUM-Neuroimaging Center, Klinikum rechts der Isar, Technical University of Munich, Munich, Germany;

[7] Department of Diagnostic and Interventional Radiology, University Hospital Ulm, Ulm, Germany;

[8] Department of Nuclear Medicine, University Hospital Ulm, Ulm, Germany.

medRxiv preprint doi: https://doi.org/10.64898/2026.06.21.26356164; this version posted June 23, 2026. The copyright holder for this preprint (which was not certified by peer review) is the author/funder, who has granted medRxiv a license to display the preprint in perpetuity.
It is made available under a CC-BY-NC 4.0 International license .

Address for correspondence:

Severin Schramm severin.schramm@tum.de

Institute for Neuroradiology

Tel.: 089/4140-7639

Klinikum rechts der Isar, Ismaninger Str. 22, 81675 Munich, Germany

Complete Contact Information:

Severin Schramm, MD severin.schramm@tum.de

Julia Ten Pas, cand. med. julia.ten-pas@tum.de

Daniele Calabro, cand. med. daniele.calabro@tum.de

Julia Jakubetz, cand. med. julia.jakubetz@tum.de

Malte Szillat, cand. med. malte.szillat@tum.de

Su Hwan Kim, MD suhwan.kim@tum.de

Jan Kirschke, MD jan.kirschke@tum.de

Dennis Hedderich, MD, MBA dennis.hedderich@tum.de

Nico Sollmann, MD, PhD nico.sollmann@tum.de

Institute for Neuroradiology

Tel.: 089/4140-4652

Klinikum rechts der Isar, Ismaninger Str. 22, 81675 Munich, Germany

Joan Koti, MD joan.koti@tum.de

medRxiv preprint doi: https://doi.org/10.64898/2026.06.21.26356164; this version posted June 23, 2026. The copyright holder for this preprint (which was not certified by peer review) is the author/funder, who has granted medRxiv a license to display the preprint in perpetuity.
It is made available under a CC-BY-NC 4.0 International license .

Ulrike Vogelmann, MD ulrike.vogelmann@tum.de

Clinic and Policlinic for Psychiatry and Psychotherapy

Tel.: 089/4140-4201

Klinikum rechts der Isar, Ismaninger Str. 22, 81675 Munich, Germany

Minyan Huang, MSc minyan.huang@meduniwien.ac.at

Michael Woletz, PhD michael.woletz@meduniwien.ac.at

Martin Tik, PhD martin.tik@meduniwien.ac.at

MR Center of Excellence

Tel.: +43 1 40160-0

Center for Medical Physics and Biomedical Engineering, Medical University of Vienna,

Spitalgasse 23, 1090 Vienna, Austria.

medRxiv preprint doi: https://doi.org/10.64898/2026.06.21.26356164; this version posted June 23, 2026. The copyright holder for this preprint (which was not certified by peer review) is the author/funder, who has granted medRxiv a license to display the preprint in perpetuity.
It is made available under a CC-BY-NC 4.0 International license .

ABSTRACT

Background: Transcranial magnetic stimulation (TMS) targeting the left dorsolateral prefrontal cortex (dlPFC) is an established treatment option in major depressive disorder. One of the most common approaches for targeting the dlPFC is the Beam F3 method, which determines the stimulation site ($F3_{Beam}$) as a function of external cranial measurements. Precise knowledge of the individual stimulation site is essential for imaging-based analyses of TMS effects. However, due to the method's reliance on individual anatomy, retrospective identification of $F3_{Beam}$ targets across cohorts is challenging, limiting the analysis of existing datasets. We developed a scalable method to reconstruct subject-specific $F3_{Beam}$ target locations for e-field simulations based on structural imaging.

Methods: High-resolution three-dimensional (3D) T1-weighted MRI was used to generate individual scalp meshes via the "Simulation of Non-Invasive Brain Stimulation" (SimNIBS) software. Subject-specific anatomical distances and coordinates of interest were measured geodesically using a Python-based script to reconstruct the individual $F3_{Beam}$ targets. Validation included a retrospective comparison between digital geodesic measurements and manual cranial measurements in 20 patients and a prospective comparison with MR-visible scalp markers in 2 healthy controls. To assess the impact of our targeting algorithm on e-field simulations, volumetric e-field maps based on three

medRxiv preprint doi: https://doi.org/10.64898/2026.06.21.26356164; this version posted June 23, 2026. The copyright holder for this preprint (which was not certified by peer review) is the author/funder, who has granted medRxiv a license to display the preprint in perpetuity.
It is made available under a CC-BY-NC 4.0 International license .

potential targets ($F3_{Beam}$, $F3_{MNI}$, $F3_{Geo}$) were generated in SimNIBS and compared using voxel-wise statistics in SPM12.

Results: Retrospective analysis revealed a systematic bias towards higher in vivo measurements compared to digital geodesic measurements, though deviations in the final distances determining $F3_{Beam}$ (x_{Beam} and y_{Beam}) were minimal (Δx_{Beam}: 0.11 ± 0.08 cm; Δy_{Beam}: 0.14 ± 0.21 cm). Prospective validation demonstrated that $F3_{Beam}$ coordinates better matched in vivo coil positions than group-template-derived targets ($F3_{MNI}$). Group-level analysis showed method-dependent clustering of coil positions with corresponding voxel-wise e-field differences.

Conclusions: Individualized geodesic measurements may enable accurate, scalable and retrospective identification of Beam F3 targets and coil orientations. This approach may yield more accurate e-field simulations than group-template based targeting and provides a practical method for retrospective analysis of existing TMS treatment cohorts. This could be leveraged to identify response predictors or imaging-based biomarkers of treatment response.

Key words: Personalization, Therapy, Individualization, Transcranial Magnetic Stimulation, Neuronavigation

medRxiv preprint doi: https://doi.org/10.64898/2026.06.21.26356164; this version posted June 23, 2026. The copyright holder for this preprint (which was not certified by peer review) is the author/funder, who has granted medRxiv a license to display the preprint in perpetuity.
It is made available under a CC-BY-NC 4.0 International license .

1. Introduction

Transcranial magnetic stimulation (TMS) is increasingly used in the therapy of a variety of psychiatric disorders [1-9]. One of the most well-established indications for TMS treatment is major depressive disorder (MDD) [1, 2, 6, 10]. The pathophysiological model underlying TMS usage presumes an imbalance between a hyperactive subgenual anterior cingulate cortex (sgACC) and hypoactive dorsolateral prefrontal cortex (dlPFC) in MDD patients [5, 10-12]. This imbalance is adressed by stimulating the left dlPFC, which indirectly inhibits the sgACC [5, 10-12].

There are several ways to identify a dlPFC stimulation target on a subject's head. While more elaborate methods incorporate functional MRI guidance and/or neuronavigation systems, one of the most common methods used is the Beam F3 method [13, 14]. In this approach, three distances are measured directly on the patient's head, i.e., tragus-tragus distance, nasion-inion distance, and head circumference. The stimulation site is then determined via two calculated target vectors x_{Beam} and y_{Beam} [13, 14]. The method has seen widespread adoption due to its ease of application [15-17].

Recent advances in TMS research leverage patient-specific electric field (e-field) modeling to infer the spatial distribution of TMS-induced effects [17-21]. By simulating how the brain's geometry and structural properties shape the TMS-induced e-field, more precise estimations of stimulated regions are made possible. This has helped to predict TMS effects both in clinical populations and healthy controls [17-21]. For example,

medRxiv preprint doi: https://doi.org/10.64898/2026.06.21.26356164; this version posted June 23, 2026. The copyright holder for this preprint (which was not certified by peer review) is the author/funder, who has granted medRxiv a license to display the preprint in perpetuity.
It is made available under a CC-BY-NC 4.0 International license .

individualized stimulation targets have been combined to inform both functional MRI and diffusion MRI analyses, enabling prediction of individual clinical outcomes in depression therapy [17, 22].

Despite enhancing imaging-based analyses, subject-specific Beam F3 localization and e-field simulations are still not widely implemented. This is likely due to the complexity of post hoc reconstruction of individual Beam F3 stimulation sites derived from multi-step manual measurements on the subjects' head. While neuroimaging in combination with dedicated MR-visible markers can address this problem [17], this requires dedicated MRI acquisitions, ideally conducted prospectively. Additionally, using a group-template-derived F3 electrode coordinate may serve as an approximation, but can introduce discrepancies due to not reflecting the actual targeting procedure [23].

A robust and scalable method for reconstructing the individual Beam F3 stimulation site using structural imaging alone could unlock retrospective analyses of large, hitherto underexplored cohorts. Additionally, it could support treatment planning and patient-specific targeting through e-field informed individualization.

To address this unmet need, we developed a method for simulating Beam F3 target locations using patient-specific scalp models and individual geodesic measurements. We describe the retrospective validation of our method in a cohort of 20 patients and prospective validation in two healthy controls (HC).

medRxiv preprint doi: https://doi.org/10.64898/2026.06.21.26356164; this version posted June 23, 2026. The copyright holder for this preprint (which was not certified by peer review) is the author/funder, who has granted medRxiv a license to display the preprint in perpetuity.
It is made available under a CC-BY-NC 4.0 International license .

2. Methods

2.1. Ethics

The imaging data utilized in this study were collected within an existing clinical study approved by the local ethics committee of the Technical University of Munich (project number: 2024-220_3-S-CB). Written informed consent for scientific usage of the acquired imaging was obtained from each study participant prior to study inclusion.

2.2. Imaging

Imaging was performed on a 3T scanner (Ingenia; Philips Medical Systems, The Netherlands B.V.) using a 32-channel head coil. Both MDD patients as well as HC underwent a sequence protocol which included a high-resolution three-dimensional (3D) T1-weighted sequence (repetition time [TR]/echo time [TE]: 9/4 ms, 1 mm^3 isovoxel covering the whole head) for structural imaging. Patients furthermore underwent a T2-like 3D magnetization transfer (MT)-weighted sequence (TR = 48 ms, $\alpha = 6°$, TE = 7 ms, MT saturation flip angle $\alpha MT = 220°$, MT pulse duration tMT = 8 ms) as part of a larger scanning protocol, which was used to supplement cortical surface reconstructions.

2.3. Geodesic Measurements

medRxiv preprint doi: https://doi.org/10.64898/2026.06.21.26356164; this version posted June 23, 2026. The copyright holder for this preprint (which was not certified by peer review) is the author/funder, who has granted medRxiv a license to display the preprint in perpetuity.
It is made available under a CC-BY-NC 4.0 International license .

The goal of the project was to create a digital step-by-step reproduction of the Beam F3 method workflow. The desired output was the determination of the $F3_{Beam}$ target and a corresponding reference direction coordinate (Ref_{Beam}, indicating coil direction) for e-field simulations.

For a given subject, $F3_{Beam}$ is found as a combination of two coordinate vectors x_{Beam} and y_{Beam}, which in turn are functions of individual anatomical distances [13].

Ref_{Beam} constitutes a point on the midline scalp which, when connected with $F3_{Beam}$ forms a 45° intersection with the midline [13].

2.3.1. Scalp Model Generation

We used the SimNIBS 4.5 charm pipeline [24] to generate individual scalp meshes from structural imaging. Cortical reconstruction was using Freesurfer-based surface segmentation (version 8.0.0) [25]. In patients, the charm pipeline was supplemented by the above mentioned T2-like imaging.

2.3.2. Geodesic Distance Measurements

The individual scalp meshes were subsequently used for geodesic measurements. The soft tissue component of the meshes was extracted from the total mesh and any mesh defects were corrected using PyMeshFix (version 0.17.1) [26] to create a watertight mesh.

medRxiv preprint doi: https://doi.org/10.64898/2026.06.21.26356164; this version posted June 23, 2026. The copyright holder for this preprint (which was not certified by peer review) is the author/funder, who has granted medRxiv a license to display the preprint in perpetuity.
It is made available under a CC-BY-NC 4.0 International license .

Geodesic distances between points of interest were computed using the PyGeodesic library (version 0.1.9) [27]. As priors, we extracted the coordinates of the following points from the SimNIBS m2mfolder: nasion (Nz), inion (Iz), left tragus (lTr), right tragus (rTr), vertex electrode (Cz), electrode positions T7, T8, and Fpz according to the SimNIBS coordinates for the 10-10 electroencephalography (EEG) system [28].

For comparison with the geodesic measurements, we also exported the F3 electrode position ($F3_{MNI}$) as output from the SimNIBS charm pipeline according to the 10-10 EEG system obtained via reverse-transformation from MNI152 space [28, 29]. The accuracy of the key anatomical landmarks (Nz, Iz, lTr and rTr) was confirmed visually by inspecting the SimNIBS head mesh for each subject. Additionally, we defined a fiducial point "EB" at one third of the geodesic path of Nz-Fpz to approximate the eyebrow level for head circumference measurement [13].

To reconstruct the manual Beam F3 targeting procedure performed on the individuals' head, we measured the distances Nz-Cz-Iz, lTr-Cz-rTr, and EB-T7-Iz-T8-EB (head circumference) on the individual scalp mesh and exported these distances to a .csv file (Figure 1B).

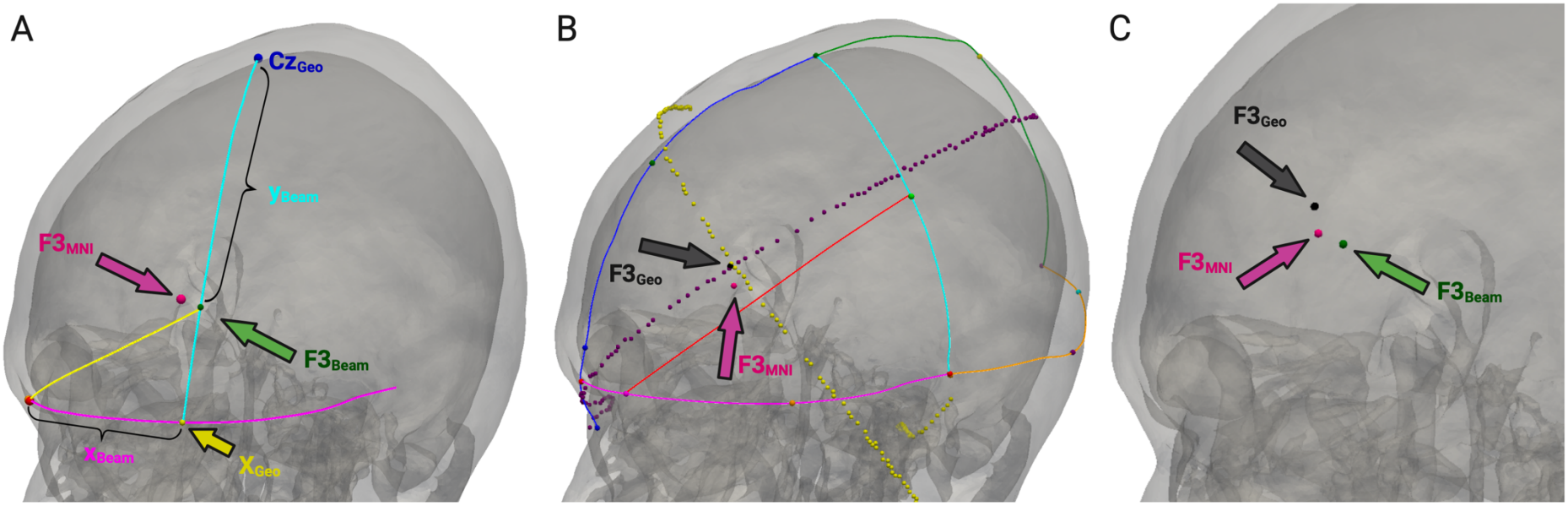


Figure 1: Exemplary Geodesic Measurements.

Figure 1 demonstrates example screenshots from the geodesic measurement process. Depicted points include $F3_{Beam}$ (Beam F3 target determined by our geodesic approach, green), $F3_{MNI}$ (F3 electrode position determined by reverse transformation from MNI152 group space, magenta) and $F3_{Geo}$ (F3 electrode position determined by geodesic approach, black).

A) Determination of $F3_{Beam}$. After calculating x_{Beam} and y_{Beam} distances, $F3_{Beam}$ (green, green arrow) is determined by going the distance x_{Beam} along the head circumference path to reach X_{Beam} (yellow dot) and subsequently going the distance y_{Beam} from Cz towards X_{Beam}.

B) Determination of $F3_{Geo}$. $F3_{Geo}$ (black arrow) is determined by calculating the intersection of equidistance lines between F7 and Fz (violet dots) as well as FP1 and C3 (yellow dots). A magenta dot (magenta arrow) indicates the position of $F3_{MNI}$, the MNI coordinate for F3 reverse-transformed into subject space.

C) Exemplary comparison of $F3_{Geo}$ (black), $F3_{MNI}$ (magenta) and $F3_{Beam}$ (green).

medRxiv preprint doi: https://doi.org/10.64898/2026.06.21.26356164; this version posted June 23, 2026. The copyright holder for this preprint (which was not certified by peer review) is the author/funder, who has granted medRxiv a license to display the preprint in perpetuity.
It is made available under a CC-BY-NC 4.0 International license .

2.3.3. Beam F3 Target Localization

We used the online tool provided in the initial publication of the Beam F3 method to input the anatomical distances for nasion-inion, tragus-tragus and head circumference (i.e., Nz-Cz-Iz, lTr-Cz-rTr, and EB-T7-Iz-T8-EB) and generate the x_{Beam} and y_{Beam} distances [13]. Specifically, we used the adjusted y_{Beam} distance (adding 0.35 cm) as established by Mir-Moghtadaei et al. [14]. The resulting x_{Beam} and y_{Beam} distances were then passed to our geodesic-based script to finalize the target determination according to the following steps: We calculated the geodesic distance of Nz-Cz-Iz and defined the midpoint (M) on this path. From M, we calculated the distance lTr-M-rTr and similarly identified the midway point on this path. This point was defined as the geodesic vertex electrode position (Cz_{Geo}). Importantly, Cz_{Geo} is approximately equidistant to both Nz and Iz as well as to lTr and rTr, marking a key reference point in the Beam F3 targeting procedure [13].

Next, we identified the point X_{Geo} by measuring the distance x_{Beam} along the path EB-T7, following the same path used in the head circumference measurement. Lastly, we identified the target $F3_{Beam}$ by measuring the distance y_{Beam} along the path Cz_{Geo}-X_{Geo} (Figure 1A). The coordinates were exported to a .csv file for further analysis.

2.3.4. Individual Geodesic Determination of F3 Electrode Position ($F3_{Geo}$)

medRxiv preprint doi: https://doi.org/10.64898/2026.06.21.26356164; this version posted June 23, 2026. The copyright holder for this preprint (which was not certified by peer review) is the author/funder, who has granted medRxiv a license to display the preprint in perpetuity.
It is made available under a CC-BY-NC 4.0 International license .

As an additional reference for comparisons, we performed an individual geodesic determination of the F3 electrode position ($F3_{Geo}$) according to the 10-10 EEG system. This yields a second, independent F3 coordinate based on the standard 10-10 layout rather than the Beam F3 method.

For this, we used the SimNIBS points Nz, Iz, lTr, rTr, and T7, as well as the previously calculated Cz_{Geo} to construct the electrode positions T3, Fz, C3, Fp1, and F7 based on geodesic measurements.

Specifically, Fz was determined at 30 % of the Nz- Cz_{Geo}-Iz distance starting from Nz; T3 was defined as the midpoint of the EB-T7-Iz path; C3 was defined as the midpoint of the Cz_{Geo}-T3 path; Fp1 was located at 10% of the EB-T7-Iz distance, starting from EB; F7 was located 30% of the EB-T7-Iz distance starting at EB.

We then defined $F3_{Geo}$ as the point equidistant to Fz and F7 as well as equidistant to C3 and Fp1 (Figure 1B).

2.3.5. Reference Direction Definition

In the Beam F3 method, coil orientation is determined by holding the coil handle in a 45° angle pointing away from the midline [13]. In clinical practice, this is achieved by using a flexible measurement tool to define the geodesic line which connects the coil center with the midline at a 45° angle.

medRxiv preprint doi: https://doi.org/10.64898/2026.06.21.26356164; this version posted June 23, 2026. The copyright holder for this preprint (which was not certified by peer review) is the author/funder, who has granted medRxiv a license to display the preprint in perpetuity.
It is made available under a CC-BY-NC 4.0 International license .

To replicate this process, we determined the coil reference direction (i.e., the direction the coil is pointing towards) by identifying the point on the path Nz-Cz_{Geo} which, when connected to $F3_{Beam}$, most closely results in a 45° intersection. This point was named Ref_{Beam} and its coordinates were exported to a .csv file. Analogous points were identified and exported by looking for a 45° intersection when connecting to the coordinates of $F3_{MNI}$ as well as $F3_{Geo}$.

2.3.6. Validation of Measurements

To validate our measurements, we employed a retrospective and a prospective comparison.

Retrospectively, we collected in-vivo scalp measurements (Nz_{viv}-Cz_{viv}-Iz_{viv}, lTr_{viv}-Cz_{viv}-rTr_{viv}, $Circumference_{viv}$, X_{viv}, and Y_{viv}) from 20 patients who had undergone depression treatment in our local psychiatry department. Head models were visually inspected to ensure absence of severe motion- or segmentation-related artifacts. We then compared these manually measured to our image-based measurements using Bland-Altman plots, concurrence correlation coefficient (CCC) analysis [30], and Passing-Bablok regression [31]. Statistical analysis was implemented in RStudio (version 2025.05.1+513) using R (version 4.5.1).

medRxiv preprint doi: https://doi.org/10.64898/2026.06.21.26356164; this version posted June 23, 2026. The copyright holder for this preprint (which was not certified by peer review) is the author/funder, who has granted medRxiv a license to display the preprint in perpetuity.
It is made available under a CC-BY-NC 4.0 International license .

Prospectively, we performed an MRI- based validation in 2 HC. Each participant underwent initial structural imaging followed by manual head measurements performed by a psychiatrist (with one year of experience in the Beam F3 targeting approach). The measured coil center and coil direction were marked using MRI-visible capsules and a second MRI scan was acquired. Points of interest ($F3_{Beam}$, $F3_{MNI}$ and their respective reference direction coordinates) were calculated based on the initial imaging and then overlaid on the coregistered marker-enhanced imaging to visualize concordance between digitally measured points and the physically marked positions.

2.3.7. Electric Field Bias Mapping

E-fields were simulated in SimNIBS 4.5 using the MagMore PMD70 coil model [32]. The maximum current gradient was set to 1,00 x 1e6 A/s. For each patient, we simulated the three calculated coil positions ($F3_{MNI}$, $F3_{Geo}$, and $F3_{Beam}$). The resulting e-fields were exported as .nifti files in both subject space and Montreal Neurological Institute (MNI)-152 space for group level analysis. Additionally, coil positions for each subject were transformed to MNI152 space and overlaid on a template to visualize clustering of coil positions across targeting methods.

We used SPM12 [33] to implement a flexible factorial statistical test design for voxel-wise comparisons of the generated e-fields. Specifically, we modeled the e-field magnitude as the dependent variable and the targeting method ($F3_{Default}$, $F3_{Geo}$, Beam F3) as a nominal

medRxiv preprint doi: https://doi.org/10.64898/2026.06.21.26356164; this version posted June 23, 2026. The copyright holder for this preprint (which was not certified by peer review) is the author/funder, who has granted medRxiv a license to display the preprint in perpetuity.
It is made available under a CC-BY-NC 4.0 International license .

factor. Analyses were performed using an explicit binary mask for the left dlPFC as previously employed by Cash et al. [3], given that e-field magnitude rapidly decreases with distance from the coil location. We generated t-contrast maps for the differences between targeting methods. A statistical threshold of $p = 0.001$ (voxel-level) and $p = 0.05$ (family-wise error-corrected, cluster level) was applied.

3. Results

3.1. Retrospective Validation

Across all measured distances, in vivo values were systematically higher than digital measurements digitally (Figure 2). Mean differences (in vivo minus digital) between measured distances were 1.23 ± 1.00 cm for Nz-Cz-Iz; 2.72 ± 0.91cm for lTr-Cz-rTR; 1.08 ± 0.66 cm for head circumference; 0.11 ± 0.08 cm for x_{Beam} and 0.14 ± 0.21 cm for y_{Beam}. Table 1 summarizes the measurements and differences between digital- and in vivo values.

The CCC analysis indicated suboptimal agreement (< 0.9 for all distance types) between in vivo and geodesic measurements (Table 2). Passing-Bablok regression indicated acceptable scaling overall (Figure 2; Table 3) with the potential exception of lTr-Cz-rTR (95 % confidence interval for slope: 0.4-0.96, excluding 1).

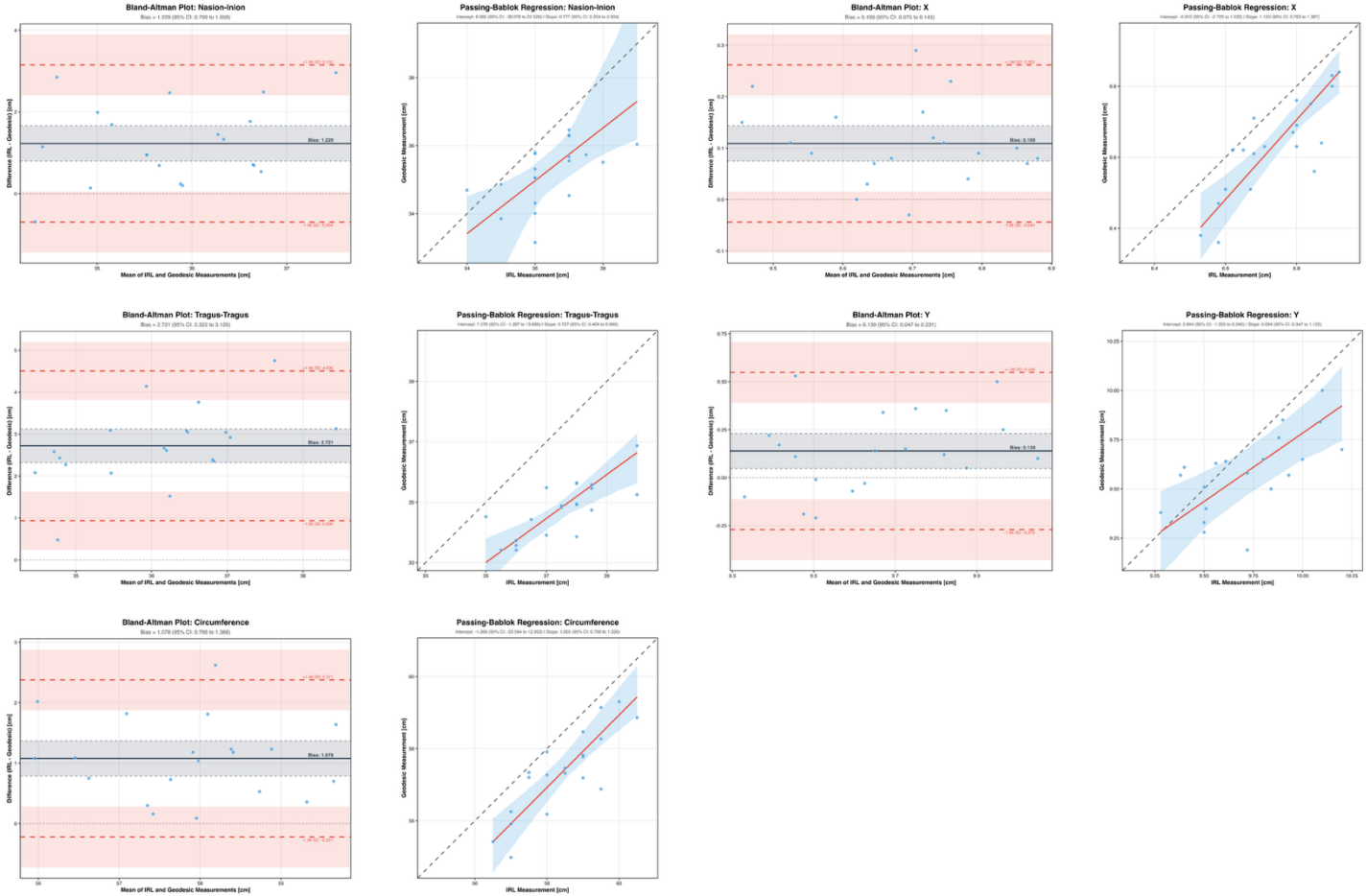


Figure 2: Bland-Altman Plots and Passing-Bablok Regressions for Geodesic and In Vivo Measurements.

Analyses reveal a systematic bias towards higher in vivo values across all anatomical distances. Despite this, scaling between in vivo and digital values was acceptable within the tested range.

medRxiv preprint doi: https://doi.org/10.64898/2026.06.21.26356164; this version posted June 23, 2026. The copyright holder for this preprint **(which was not certified by peer review)** is the author/funder, who has granted medRxiv a license to display the preprint in perpetuity.
It is made available under a CC-BY-NC 4.0 International license .

3.2. Prospective Validation

$F3_{Beam}$ demonstrated better overlap with the in vivo marked points compared to $F3_{MNI}$. In both individuals, $F3_{Beam}$ was located within the marker structure, while $F3_{MNI}$ remained more anterior. Coil direction as indicated by Ref_{Beam}, was highly comparable to the reference direction measured in vivo (Figure 3).

medRxiv preprint doi: https://doi.org/10.64898/2026.06.21.26356164; this version posted June 23, 2026. The copyright holder for this preprint (which was not certified by peer review) is the author/funder, who has granted medRxiv a license to display the preprint in perpetuity.
It is made available under a CC-BY-NC 4.0 International license .

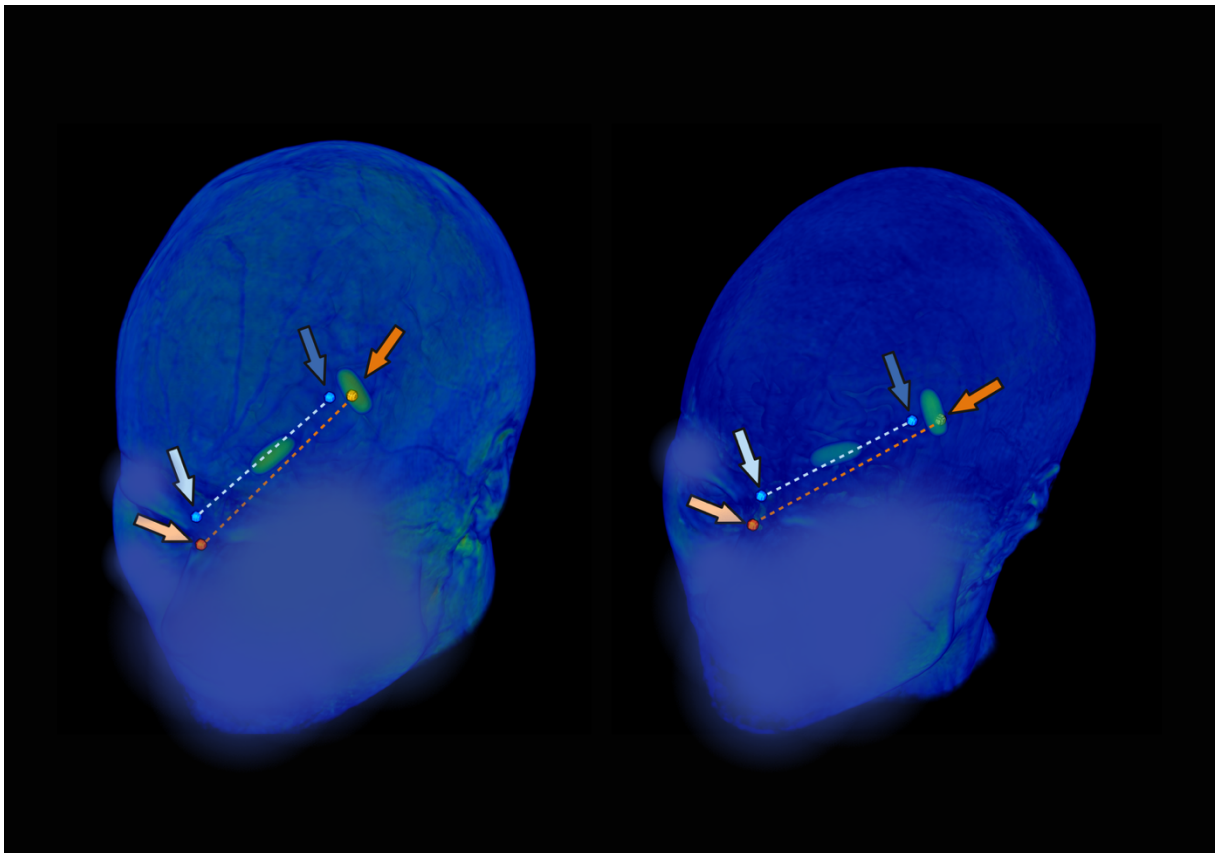


Figure 3: Prospective Targeting Validation.

Scalp reconstructions with overlayed target coordinates. MRI markers on the scalp in green indicate the physically marked positions for coil center and reference direction. Blue points and arrows indicate $F3_{MNI}$ and its corresponding reference target for 45° coil orientation (blue dotted line); orange points and arrows indicate $F3_{Beam}$ and Ref_{Beam} points. In both subjects, $F3_{Beam}$ lies within the marker structure while $F3_{MNI}$ is located anterior to the marker. Of note, the dotted lines are overlaid projections and do not reflect the true 3D path on the head surface used in the reference point calculations.

medRxiv preprint doi: https://doi.org/10.64898/2026.06.21.26356164; this version posted June 23, 2026. The copyright holder for this preprint (which was not certified by peer review) is the author/funder, who has granted medRxiv a license to display the preprint in perpetuity.
It is made available under a CC-BY-NC 4.0 International license .

3.3. Electric-Field Bias Mapping

Voxel-wise comparisons of e-fields based on $F3_{MNI}$, $F3_{Geo}$, and $F3_{Beam}$ indicated significant differences in simulated e-field distributions, corresponding to the observed clustering of coil positions (Figure 4). While $F3_{MNI}$ naturally converged to a single MNI space coordinate at the group level, $F3_{Geo}$ clusters were located more posteriorly, and $F3_{Beam}$ positions more posterior-inferiorly. Consequently, $F3_{MNI}$ resulted in systematically higher e-fields in the superior-anterior dlPFC, and lower e-fields them in the posterior-inferior dlPFC compared to $F3_{Beam}$ (Figure 4). A medial-lateral bias was observed when comparing $F3_{Geo}$ derived e-fields to $F3_{Beam}$ e-fields (Figure 4).

medRxiv preprint doi: https://doi.org/10.64898/2026.06.21.26356164; this version posted June 23, 2026. The copyright holder for this preprint (which was not certified by peer review) is the author/funder, who has granted medRxiv a license to display the preprint in perpetuity.
It is made available under a CC-BY-NC 4.0 International license .

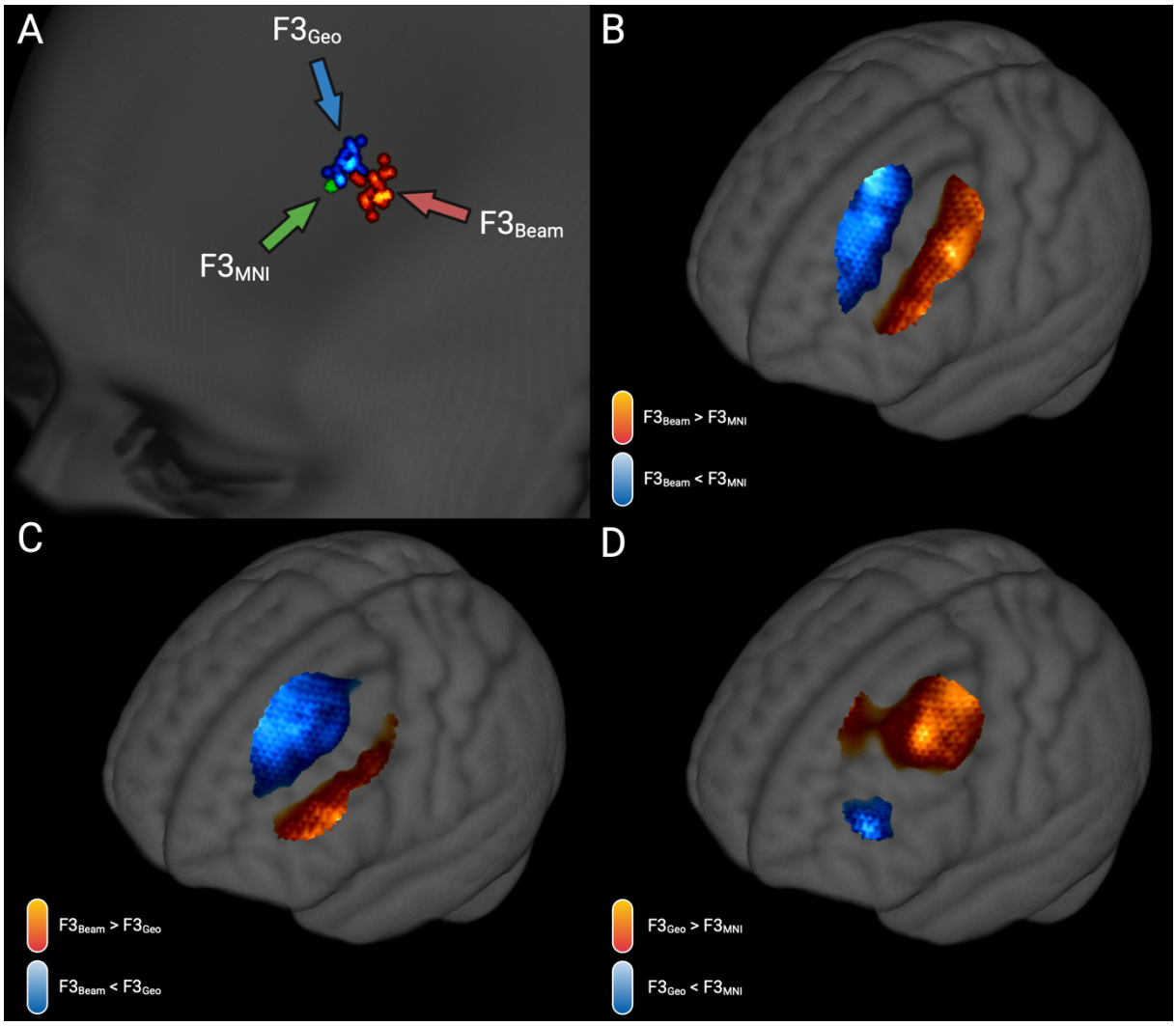


Figure 4: Target Locations at the Group Level and E-Field Biases.

A) Targets positions by method overlaid onto an MNI152 template scalp. The green point (green arrow) indicates $F3_{MNI}$, which converges to a single MNI152 coordinate across subjects. Red points (red arrow) indicate $F3_{Beam}$ coordinates, clustering more posterior and inferior compared to $F3_{MNI}$. Blue points (blue arrow) indicate coordinates for $F3_{Geo}$, clustering slightly more posterior compared to $F3_{MNI}$.

B) Thresholded T-contrast for E-fields of $F3_{Beam}$ vs. $F3_{MNI}$. The warm-colored cluster indicates areas with higher e-field magnitude for $F3_{Beam}$, while the cool-colored cluster indicates areas with lower e-field magnitude for $F3_{Beam}$. A threshold of voxel-level $p < 0.001$, cluster-level $p < 0.05$ FWE-corrected was applied.

medRxiv preprint doi: https://doi.org/10.64898/2026.06.21.26356164; this version posted June 23, 2026. The copyright holder for this preprint (which was not certified by peer review) is the author/funder, who has granted medRxiv a license to display the preprint in perpetuity.
It is made available under a CC-BY-NC 4.0 International license .

C) Thresholded T-contrast for E-fields of $F3_{Beam}$ vs. $F3_{Geo}$. The warm-colored cluster indicates areas with higher e-field magnitude for $F3_{Beam}$, while the cool-colored cluster indicates areas with lower e-field magnitude for $F3_{Beam}$. A threshold of voxel-level $p < 0.001$, cluster-level $p < 0.05$ FWE-corrected was applied.

D) Thresholded T-contrast for E-fields of $F3_{Geo}$ vs. $F3_{MNI}$. The warm-colored cluster indicates areas with higher e-field magnitude for $F3_{MNI}$, while the cool-colored cluster indicates areas with lower e-field magnitude for $F3_{MNI}$. A threshold of voxel-level $p < 0.001$, cluster-level $p < 0.05$ FWE-corrected was applied.

4. Discussion

We present a method for retrospective identification of Beam F3 TMS targets based on individualized geodesic scalp measurements. Our results indicate that this individualized method provides more accurate coil positions than group-level MNI-based targeting of the F3 electrode position (Figure 3), and that group-level assumptions may introduce systemic biases in calculated e-fields (Figure 4).

4.1. Measurement Validity

Our retrospective comparison of digitally measured values and in vivo values yielded mixed results. The CCC analysis suggested poor reliability, which we interpret as largely reflecting a systematic upward bias in the in vivo measurements. However, inspection of the Passing-Bablok regression plots indicated that geodesic distances were well scaled across the observed ranges despite an overall shift towards lower digital values.

We suspect that the higher in vivo values arise from how the measurement procedure is implemented in vivo. Our mesh-based approach measures directly on the scalp, whereas in vivo measurements are usually performed with subjects wearing a textile cap that compresses hair

medRxiv preprint doi: https://doi.org/10.64898/2026.06.21.26356164; this version posted June 23, 2026. The copyright holder for this preprint (which was not certified by peer review) is the author/funder, who has granted medRxiv a license to display the preprint in perpetuity.
It is made available under a CC-BY-NC 4.0 International license .

and adds an additional layer on top of the scalp. This likely results in higher distances across all measurements. Importantly, for the Beam F3-relevant distances x_{Beam} and y_{Beam}, deviations from the in vivo values were minimal and remained in the low millimeter range (Table 1). Furthermore, prospective validation direct distance comparisons showed that our approach approximates the Beam F3 targeting procedure more accurately than MNI-based targeting of the F3 electrode position (Figure 3). Additionally, our process is fully deterministic and can be tailored towards other targets such as alternative EEG coordinates.

4.2. Use Cases

Although neuronavigation of TMS is becoming increasingly common, non-navigated application of stimulation remains widespread globally due to its lower cost and ease of application. In this context, an accurate way to retrospectively simulate the individual e-field applied during therapy could unlock large cohorts for add-on analyses, enabling more sophisticated investigations of potential response predictors and imaging-based biomarkers of treatment response such as functional or structural connectivity patterns specific to the individually stimulated cortical areas. Importantly, e-field intensity is assumed to influence clinical outcome [34, 35]. Therefore, precise e-field modeling is crucial, as the strength of the induced e-field at the intended target, typically the dlPFC, may directly affect clinical outcomes. Inaccurate localization of the stimulation site can lead to substantial deviations in the modeled e-field intensity at the target region, thereby confounding the interpretation of dose–response relationships. Consequently, improving the precision of e-field estimation at the true stimulation site is essential for reliably assessing and potentially optimizing the clinical efficacy of TMS interventions.

A prior study had already indicated discrepancies between the Beam F3 target and the F3 electrode spot according to the 10-20 EEG system [23]. Our results similarly show that $F3_{Beam}$ coordinates cluster distinctly from both $F3_{MNI}$ and $F3_{Geo}$ coordinates, with corresponding biases

medRxiv preprint doi: https://doi.org/10.64898/2026.06.21.26356164; this version posted June 23, 2026. The copyright holder for this preprint (which was not certified by peer review) is the author/funder, who has granted medRxiv a license to display the preprint in perpetuity.
It is made available under a CC-BY-NC 4.0 International license .

in the simulated e-field (Figure 4). One of the advantages of using personalized measurements is exemplified here: target locations cluster around a given spot yet vary more across individuals than can be captured in a single MNI coordinate (Figure 4). Previous work has already demonstrated the predictive power of individualized e-field mappings in various contexts [17, 18, 36, 37]. However, these approaches have hitherto relied on either neuronavigation or marker-based recordings of stimulation sites [17, 18, 36, 37].

4.3. Limitations

Physical measurements are usually performed on the patient's head, often over a cap, rather than directly on the scalp, which may introduce a bias in our method regarding the measurements of Nz_{viv}-Cz_{viv}-Iz_{viv}, lTr_{viv}-Cz_{viv}-rTr_{viv} and $Circumference_{viv}$. Nonetheless, our results suggest a meaningful improvement over non-individualized, MNI-based targeting, better reflecting the actual stimulation sites and thus generating more accurate, individualized e-field maps.

Second, our approach relies on high-quality structural imaging, including at least a high-resolution 3D T1-weighted sequence and appropriate segmentation of mesh components in the SimNIBS charm pipeline. Although we cannot provide e-fields for patients with no imaging data at all, recent advances in the field of synthetic MRI [38] could potentially generate individual high-resolution T1-weighted imaging for patient with lower resolution data, and thus provide an avenue for geodesic Beam F3 targeting reconstruction.

Third, our approach relies on multiple starting coordinates (e.g., Nz, Iz, lTr, or rTr), which are by default extracted from SimNIBS and thus are reverse-transformed from MNI152 space. This implementation allows efficient batch processing but is dependent on accurate transformations between spaces. Manual identification of these above-mentioned reference coordinates could potentially improve subject-specific accuracy but would come at the cost of added time required to visually identify the respective landmarks.

medRxiv preprint doi: https://doi.org/10.64898/2026.06.21.26356164; this version posted June 23, 2026. The copyright holder for this preprint (which was not certified by peer review) is the author/funder, who has granted medRxiv a license to display the preprint in perpetuity.
It is made available under a CC-BY-NC 4.0 International license .

5. Conclusion

We present a method for accurate and individualized identification of the Beam F3 target and coil orientation based on structural imaging. This may allow for retrospective simulation of applied e-fields in TMS applications, such as for the treatment of depression. Our results indicate that this method yields more accurate e-field simulations than MNI-based targeting, and results in systematically different e-fields. This method can be employed to retrospectively investigate cohorts regarding potential response predictors or therapy-associated imaging markers for TMS.

6. Acknowledgements

None.

7. Disclosures

-

8. References

1. Rossi S, Antal A, Bestmann S, et al. Safety and recommendations for TMS use in healthy subjects and patient populations, with updates on training, ethical and regulatory issues: Expert Guidelines. Clin Neurophysiol 2021;132:269–306.
2. Cash RF, Cocchi L, Lv J, Fitzgerald PB, Zalesky A. Functional magnetic resonance imaging–guided personalization of transcranial magnetic stimulation treatment for depression. JAMA psychiatry 2021;78:337–339.
3. Cash RF, Cocchi L, Lv J, Wu Y, Fitzgerald PB, Zalesky A. Personalized connectivity-guided DLPFC-TMS for depression: Advancing computational feasibility, precision and reproducibility. Hum Brain Mapp 2021;42:4155–4172.
4. Fitzgerald PB. Targeting repetitive transcranial magnetic stimulation in depression: do we really know what we are stimulating and how best to do it? Brain Stimul 2021;14:730–736.
5. Fox MD, Buckner RL, White MP, Greicius MD, Pascual-Leone A. Efficacy of transcranial magnetic stimulation targets for depression is related to intrinsic functional connectivity with the subgenual cingulate. Biol Psychiatry 2012;72:595–603.

medRxiv preprint doi: https://doi.org/10.64898/2026.06.21.26356164; this version posted June 23, 2026. The copyright holder for this preprint (which was not certified by peer review) is the author/funder, who has granted medRxiv a license to display the preprint in perpetuity.
It is made available under a CC-BY-NC 4.0 International license .

6. Blumberger DM, Vila-Rodriguez F, Thorpe KE, et al. Effectiveness of theta burst versus high-frequency repetitive transcranial magnetic stimulation in patients with depression (THREE-D): a randomised non-inferiority trial. The Lancet 2018;391:1683–1692.
7. Chu C-S, Li C-T, Brunoni AR, et al. Cognitive effects and acceptability of non-invasive brain stimulation on Alzheimer's disease and mild cognitive impairment: a component network meta-analysis. J Neurol Neurosurg Psychiatry 2021;92:195–203.
8. Mehta DD, Siddiqui S, Ward HB, Steele VR, Pearlson GD, George TP. Functional and structural effects of repetitive transcranial magnetic stimulation (rTMS) for the treatment of auditory verbal hallucinations in schizophrenia: a systematic review. Schizophr Res 2024;267:86–98.
9. Vicheva P, Osborne C, Krieg SM, Ahmadi R, Shotbolt P. Transcranial magnetic stimulation for obsessive-compulsive disorder and post-traumatic stress disorder: A comprehensive systematic review and analysis of therapeutic benefits, cortical targets, and psychopathophysiological mechanisms. Prog Neuropsychopharmacol Biol Psychiatry 2025;136:111147.
10. Cole EJ, Phillips AL, Bentzley BS, et al. Stanford neuromodulation therapy (SNT): a double-blind randomized controlled trial. Am J Psychiatry 2022;179:132–141.
11. Fox MD, Liu H, Pascual-Leone A. Identification of reproducible individualized targets for treatment of depression with TMS based on intrinsic connectivity. Neuroimage 2013;66:151–160.
12. Klooster D, Voetterl H, Baeken C, Arns M. Evaluating robustness of brain stimulation biomarkers for depression: A systematic review of magnetic resonance imaging and electroencephalography studies. Biol Psychiatry 2024;95:553–563.
13. Beam W, Borckardt JJ, Reeves ST, George MS. An efficient and accurate new method for locating the F3 position for prefrontal TMS applications. Brain Stimul 2009;2:50–54.
14. Mir-Moghtadaei A, Caballero R, Fried P, et al. Concordance between BeamF3 and MRI-neuronavigated target sites for repetitive transcranial magnetic stimulation of the left dorsolateral prefrontal cortex. Brain Stimul 2015;8:965–973.
15. Trapp NT, Bruss J, Johnson MK, et al. Reliability of targeting methods in TMS for depression: Beam F3 vs. 5.5 cm. Brain Stimul 2020;13:578–581.
16. Trapp NT, Pace BD, Neisewander B, Ten Eyck P, Boes AD. A randomized trial comparing beam F3 and 5.5 cm targeting in rTMS treatment of depression demonstrates similar effectiveness. Brain Stimul 2023;16:1392–1400.
17. Rajasekharan D, Madore MR, Holtzheimer P, Lim KO, Williams LM, Philip NS. Personalized models of Beam/F3 targeting in transcranial magnetic stimulation for depression: Implications for precision clinical translation. Brain Stimul 2025;18:829–837.
18. Numssen O, Kuhnke P, Weise K, Hartwigsen G. Electric-field-based dosing for TMS. Imaging Neuroscience 2024;2:1–12.
19. Weise K, Makaroff SN, Numssen O, Bikson M, Knösche TR. Statistical method accounts for microscopic electric field distortions around neurons when simulating activation thresholds. Brain Stimul 2025.
20. Dannhauer M, Gomez LJ, Robins PL, et al. Electric Field Modeling in Personalizing Transcranial Magnetic Stimulation Interventions. Biol Psychiatry 2024;95:494–501.
21. Gomez LJ, Dannhauer M, Peterchev AV. Fast computational optimization of TMS coil placement for individualized electric field targeting. Neuroimage 2021;228:117696.
22. Seguin C, Mansour L S, Betzel RF, et al. Neuroanatomical pathways of TMS therapy for depression. medRxiv 2025:2025.2002. 2010.25322034.
23. Fabregat-Sanjuan A, Pàmies-Vilà R, Pascual-Rubio V. Evaluation of the Beam-F3 method for locating the F3 position from the 10–20 international system. Brain Stimul 2022;15:1011–1012.

medRxiv preprint doi: https://doi.org/10.64898/2026.06.21.26356164; this version posted June 23, 2026. The copyright holder for this preprint (which was not certified by peer review) is the author/funder, who has granted medRxiv a license to display the preprint in perpetuity.
It is made available under a CC-BY-NC 4.0 International license .

24. Puonti O, Van Leemput K, Saturnino GB, Siebner HR, Madsen KH, Thielscher A. Accurate and robust whole-head segmentation from magnetic resonance images for individualized head modeling. Neuroimage 2020;219:117044.
25. Fischl B. FreeSurfer. Neuroimage 2012;62:774–781.
26. Attene M. A lightweight approach to repairing digitized polygon meshes. The visual computer 2010;26:1393–1406.
27. Hogg M, Kaszynski A. pygeodesic (V. 0.1.9) [online]. Available at: https://github.com/mhogg/pygeodesic. Accessed 01.06.2025.
28. Jurcak V, Tsuzuki D, Dan I. 10/20, 10/10, and 10/5 systems revisited: their validity as relative head-surface-based positioning systems. Neuroimage 2007;34:1600–1611.
29. Saturnino GB, Puonti O, Nielsen JD, Antonenko D, Madsen KH, Thielscher A. SimNIBS 2.1: a comprehensive pipeline for individualized electric field modelling for transcranial brain stimulation. Brain and human body modeling: computational human modeling at EMBC 2018 2019:3–25.
30. Lawrence I, Lin K. A concordance correlation coefficient to evaluate reproducibility. Biometrics 1989:255–268.
31. Passing H, Bablok W. A new biometrical procedure for testing the equality of measurements from two different analytical methods. Application of linear regression procedures for method comparison studies in clinical chemistry, Part I. 1983.
32. Drakaki M, Mathiesen C, Siebner HR, Madsen K, Thielscher A. Database of 25 validated coil models for electric field simulations for TMS. Brain Stimul 2022;15:697–706.
33. Friston KJ, Holmes AP, Worsley KJ, Poline JP, Frith CD, Frackowiak RS. Statistical parametric maps in functional imaging: a general linear approach. Hum Brain Mapp 1994;2:189–210.
34. Zhang R, Lam CL, Peng X, et al. Efficacy and acceptability of transcranial direct current stimulation for treating depression: a meta-analysis of randomized controlled trials. Neurosci Biobehav Rev 2021;126:481–490.
35. Deng Z-D, Robins PL, Dannhauer M, Haugen LM, Port JD, Croarkin PE. Optimizing TMS coil placement approaches for targeting the dorsolateral prefrontal cortex in depressed adolescents: an electric field modeling study. Biomedicines 2023;11:2320.
36. Quinn DK, Upston J, Jones TR, et al. Electric field distribution predicts efficacy of accelerated intermittent theta burst stimulation for late-life depression. Frontiers in Psychiatry 2023;14:1215093.
37. Harita S, Momi D, Mazza F, Griffiths JD. Mapping inter-individual functional connectivity variability in TMS targets for major depressive disorder. Frontiers in Psychiatry 2022;13:902089.
38. Iglesias JE, Billot B, Balbastre Y, et al. SynthSR: A public AI tool to turn heterogeneous clinical brain scans into high-resolution T1-weighted images for 3D morphometry. Science advances 2023;9:eadd3607.

9. Tables

Table 1: Overview of Distances Measured in Vivo and Digitally

Distance	In Vivo Measurement; Mean ± SD [cm]	Digital Measurement; Mean ± SD [cm]	Delta of Measurements; Mean ± SD [cm]
Nasion-Inion	36.43 ± 1.12	35.20 ± 0.90	1.23 ± 1.00
Tragus-Tragus	37.48 ± 1.36	34.75 ± 0.91	2.72 ± 0.91
Circumference	58.43 ± 1.12	57.35 ± 1.2	1.08 ± 0.66
$\mathbf{X_{Beam}}$	6.74 ± 0.12	6.63 ± 0.14	0.11 ± 0.08
$\mathbf{Y_{Beam}}$	9.72 ± 0.27	9.58 ± 0.20	0.14 ± 0.21

Table 1 summarizes the distances measured in vivo and their corresponding digital geodesic measurements. Abbreviations: standard deviation (SD).

Table 2: Concordance Correlation Coefficient Analysis

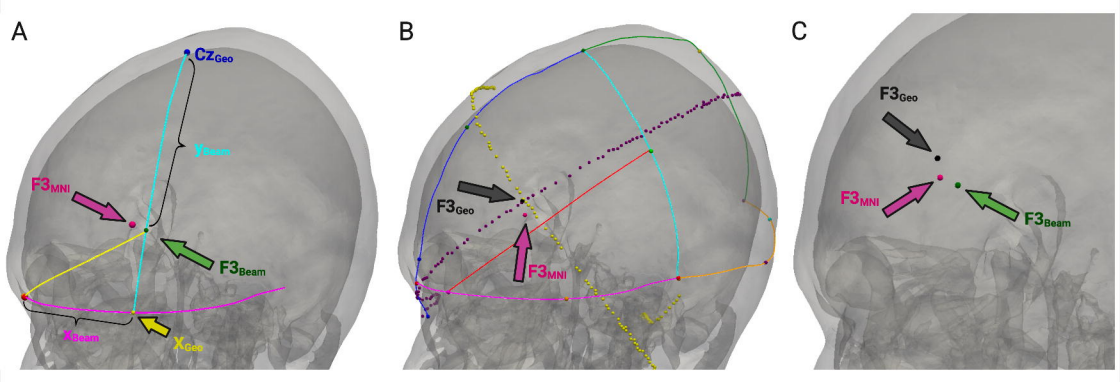
Distance	CCC Estimate and 95% CI	Pearson Correlation Coefficient
Nasion-Inion	0.30 [0.04; 0.52]	0.54
Tragus-Tragus	0.18 [0.06; 0.29]	0.75
Circumference	0.57 [0.32; 0.74]	0.83
X_{Beam}	0.60 [0.34; 0.77]	0.82
Y_{Beam}	0.52 [0.19; 0.74]	0.63

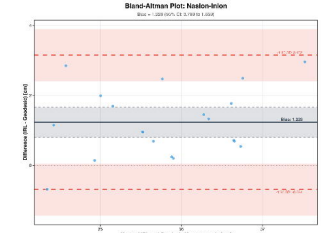
Table 2 summarizes the metrics from the Concordance Correlation Coefficient (CCC) analysis comparing the in vivo distances with their corresponding digital geodesic measurements. Abbreviations: Concordance Correlation Coefficient (CCC), confidence interval (CI).

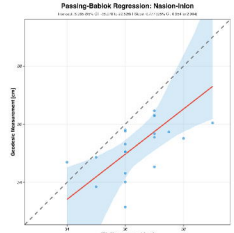
Table 3: Passing-Bablok Regression

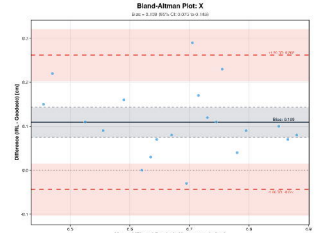
Distance	Intercept and 95% CI	Slope and 95% CI
Nasion-Inion	6.99 [-38.08; 22.53]	0.78 [0.35; 2.00]
Tragus-Tragus	7.58 [-1.40; 19.70]	0.73 [0.40; 0.96]
Circumference	-1.37 [-20.59; 12.95]	1.00 [0.76; 1.33]
X_{Beam}	-0.91 [-2.73; 1.53]	1.12 [0.76; 1.39]
Y_{Beam}	2.84 [-1.36; 6.24]	0.69[0.35; 1.13]

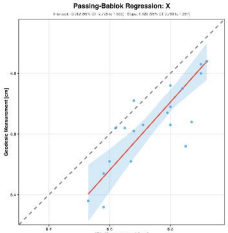
Table 3 summarizes the metrics from the Passing-Bablok regression comparing the in vivo distances with their corresponding digital geodesic measurements. In the Passing-Bablok regression, an intercept $\neq 0$ indicates a systematic bias, while the slope indicates whether scaling is comparable across the two measurement methods with 1 indicating perfect scaling. Abbreviations: Confidence interval (CI).

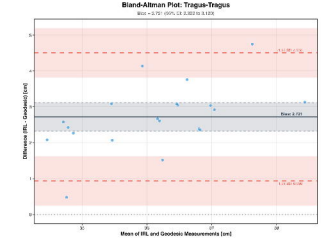

A
Cz Geo
Y Beam
F3 MNI
F3 Beam
X Beam
X Geo
B
F3 Geo
F3 MNI
C
F3 Geo
F3 MNI
F3 Beam

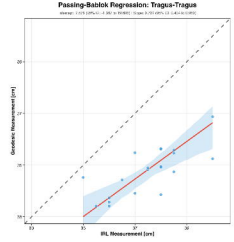

Bland-Altman Plot: Nasion-Inion
Bias = 1.329 (95% CI: 1.193 to 1.464)
Bias: 1.329
Mean of IRL and Geodesic Measurements [cm]
Difference (IRL - Geodesic) [cm]

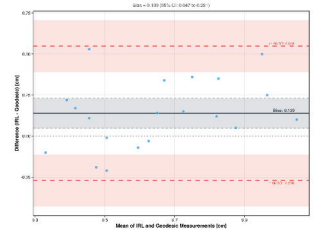

Passing-Bablok Regression: Nasion-Inion
IRL Measurement [cm]
Geodesic Measurement [cm]

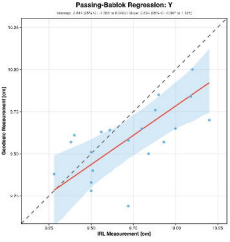

Bland-Altman Plot: X
Bias = 0.038 (95% CI: 0.013 to 0.062)
Bias: 0.038
Mean of IRL and Geodesic Measurements [cm]
Difference (IRL - Geodesic) [cm]

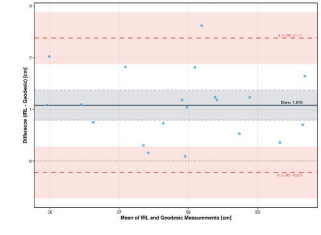

Passing-Bablok Regression: X
IRL Measurement [cm]
Geodesic Measurement [cm]

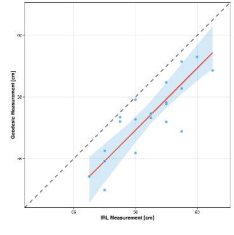

Bland-Altman Plot: Tragus-Tragus
Bias = 2.751 (95% CI: 2.502 to 3.000)
Bias: 2.751
Mean of IRL and Geodesic Measurements [cm]
Difference (IRL - Geodesic) [cm]

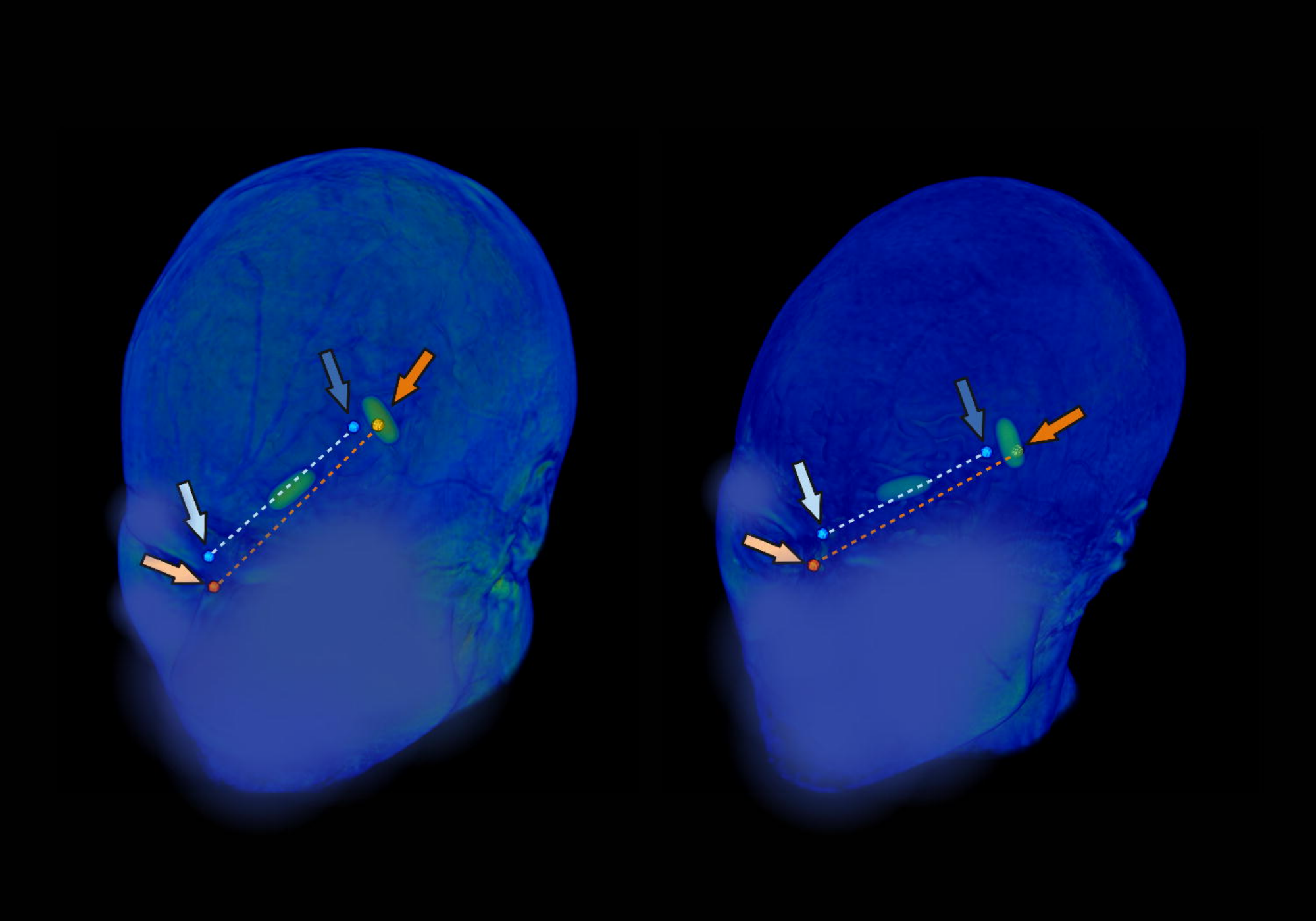

Passing-Bablok Regression: Tragus-Tragus
IRL Measurement [cm]
Geodesic Measurement [cm]

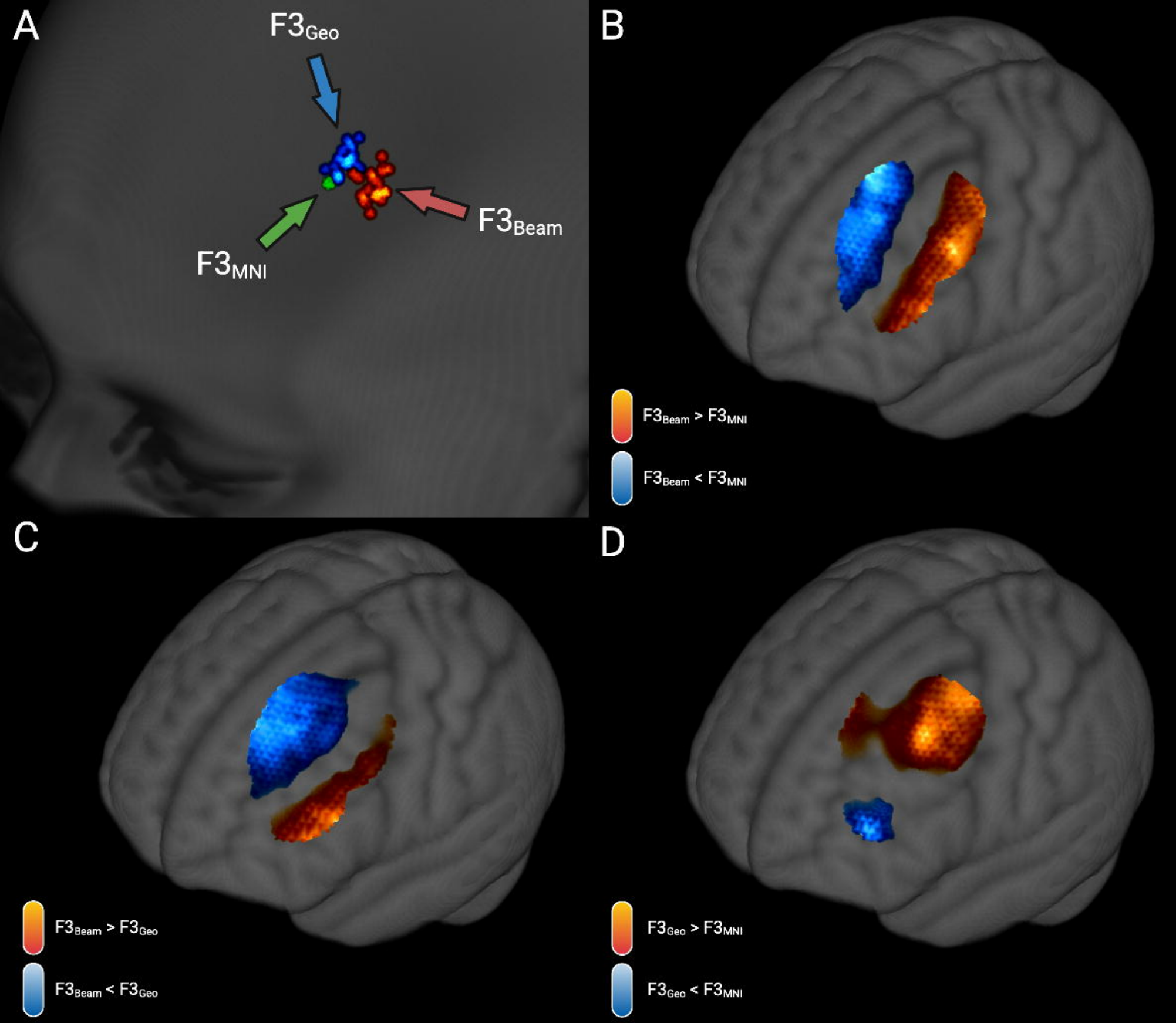

Bland-Altman Plot: Y
Bias = 0.332 (95% CI: 0.067 to 0.597)
Bias: 0.332
Mean of IRL and Geodesic Measurements [cm]
Difference (IRL - Geodesic) [cm]


Passing-Bablok Regression: Y
IRL Measurement [cm]
Geodesic Measurement [cm]


Bland-Altman Plot: Circumference
Bias = 1.878 (95% CI: 0.789 to 1.968)
Bias: 1.878
Mean of IRL and Geodesic Measurements [cm]
Difference (IRL - Geodesic) [cm]


Passing-Bablok Regression: Circumference
IRL Measurement [cm]
Geodesic Measurement [cm]




A
F3Geo
F3Beam
F3MNI
B
F3Beam > F3MNI
F3Beam < F3MNI
C
F3Beam > F3Geo
F3Beam < F3Geo
D
F3Geo > F3MNI
F3Geo < F3MNI